RSC Advances

PAPER

View Article Online
View Journal | View Issue

Check for updates

Cite this: *RSC Adv.*, 2022, **12**, 10020

Steps towards highly-efficient water splitting and oxygen reduction using nanostructured β-Ni(OH)$_2$

Aldona Balčiūnaitė,†[a] Kush K. Upadhyay,†[b] Kristina Radinović,[c]
Diogo M. F. Santos,[d] M. F. Montemor[b] and Biljana Šljukić*[cd]

Received 11th February 2022
Accepted 20th March 2022

DOI: 10.1039/d2ra00914e

rsc.li/rsc-advances

β-Ni(OH)$_2$ nanoplatelets are prepared by a hydrothermal procedure and characterized by scanning and transmission electron microscopy, X-ray diffraction analysis, Raman spectroscopy, and X-ray photoelectron spectroscopy. The material is demonstrated to be an efficient electrocatalyst for oxygen reduction, oxygen evolution, and hydrogen evolution reactions in alkaline media. β-Ni(OH)$_2$ shows an overpotential of 498 mV to reach 10 mA cm^{-2} towards oxygen evolution, with a Tafel slope of 149 mV dec^{-1} (decreasing to 99 mV dec^{-1} at 75 °C), along with superior stability as evidenced by chronoamperometric measurements. Similarly, a low overpotential of −333 mV to reach 10 mA cm^{-2} (decreasing to only −65 mV at 75 °C) toward hydrogen evolution with a Tafel slope of −230 mV dec^{-1} is observed. Finally, β-Ni(OH)$_2$ exhibits a noteworthy performance for the ORR, as evidenced by a low Tafel slope of −78 mV dec^{-1} and a number of exchanged electrons of 4.01 (indicating direct 4e$^-$-oxygen reduction), whereas there are only a few previous reports on modest ORR activity of pure Ni(OH)$_2$.

1. Introduction

Nickel (Ni)-based materials, including nickel alloys, oxides, hydroxides, and oxyhydroxides, exhibit exceptional electrocatalytic performance for the most relevant reactions occurring in electrochemical energy storage and conversion devices.[1] Unlike Ni, which is easily oxidized when in contact with air or aqueous solutions,[2] Ni (oxo)hydroxides are very stable and have been reported to have better electrocatalytic performance than NiO. Different electrocatalytic mechanisms have been proposed: Ni(OH)$_2$/NiOOH mediated electrolysis and direct electrocatalysis of Ni(OH)$_2$ or NiOOH. The electrocatalytic activity of NiOOH towards the oxidation of small molecules most likely originates in the presence of unpaired d-electrons or empty d-orbitals that enable the formation of bonds with adsorbed or intermediate species.[3,4] Furthermore, Ni (oxo) hydroxides have been reported to have excellent activity toward the oxygen evolution reaction (OER), a key reaction in many electrochemical energy conversion processes.[5–7] For instance, the OER proceeds at the anode during water splitting (used to produce hydrogen gas at the cathode), and it is the limiting reaction involving a multistep proton-coupled electron transfer. The OER's sluggish kinetics result in higher overpotential to overcome the large energy barrier[8] and increased cell voltage for water splitting, compared to the theoretical value of 1.23 V. Thus, Ni-based (oxo)hydroxides (NiFe-based (oxy)hydroxides,[9] Ni(OH)$_2$/NiOOH),[10] Ni sulfides (FeNiS$_2$),[11] nitrides (Ni$_3$N/Ni),[12] phosphides (Ni–Fe$_x$P),[13] and selenides (Ni$_3$Se$_2$ and Ni$_x$Fe$_{1-x}$Se$_2$)[14,15] have been tested for OER and observed to reach high current densities at low overpotentials, along with high stability. Ni(OH)$_2$ catalysts of different morphologies have been prepared by a co-precipitation method revealing higher OER activity of the nanostructured Ni(OH)$_2$ compared to the bulk one.[16] This higher performance toward OER of Ni(OH)$_2$ nanoparticles was correlated with their ultra-fine size, leading to a higher number of active faces/edges. These nanoparticles were reported to reduce OER overpotential by 300 mV.[16] Similarly, β-Ni(OH)$_2$ nanoplates array on NiAl foil demonstrated good OER electrocatalytic performance.[17] Two-dimensional nanosheet morphology was also beneficial for Ni(OH)$_2$ electrocatalytic activity by providing a high specific surface area and a short ion-diffusion distance.[1] When it comes to different structures of Ni(OH)$_2$ catalysts, α-Ni(OH)$_2$ has previously shown higher performance during OER compared to β-Ni(OH)$_2$, which was correlated with its higher interlayer space. Additionally, α-Ni(OH)$_2$ typically transforms to γ-NiOOH during the electrochemical process, with this α-Ni(OH)$_2$/γ-NiOOH pair delivering a higher number of electrons compared to β-Ni(OH)$_2$/β-NiOOH pair.[16]

---

[a] *Department of Catalysis, Center for Physical Sciences and Technology, Saulėtekio ave. 3, Vilnius LT-10257, Lithuania*

[b] *Centro de Química Estrutural-CQE, Institute of Molecular Sciences, Departamento de Engenharia Química, Instituto Superior Técnico, Universidade de Lisboa, 1049-001 Lisbon, Portugal*

[c] *University of Belgrade, Faculty of Physical Chemistry, Studentski trg 12-16, 11158 Belgrade, Serbia. E-mail: biljana.paunkovic@tecnico.ulisboa.pt*

[d] *Center of Physics and Engineering of Advanced Materials, Laboratory for Physics of Materials and Emerging Technologies, Chemical Engineering Department, Instituto Superior Técnico, Universidade de Lisboa, 1049-001 Lisbon, Portugal*

† Equally contributed.

For complete water splitting to produce simultaneously hydrogen and oxygen gases, cathodic (hydrogen evolution reaction, HER) and anodic (OER) reactions should be efficient in the same electrolytic solution.[18–20] The disparity of the conditions under which the electrocatalyst effectively operates is responsible for a decrease in the efficiency of the water-splitting process.[21–23] Materials with electrocatalytic activity toward HER typically show better performance in acidic electrolytes, while those with activity toward OER generally show good performance in alkaline electrolytes. Building bifunctional electrocatalysts with high efficiency for both hydrogen and oxygen evolution, as well as stability in the same electrolytic solution, has been marked to be of utter importance. As mentioned above, the electrocatalyst's structure and morphology should be designed to display large electrochemically active surface area, fast charge transfer, and gas transport. These properties are necessary to achieve high electrocatalytic activity, decrease the overpotential of the evolution reactions, and enhance the reaction kinetics. Overall, this leads, finally, to a significant increase in the water-splitting process efficiency.[23,24]

Besides the two reactions (OER and HER) involved in water splitting, the oxygen reduction reaction (ORR) is vital in electrochemical energy storage/conversion devices, such as fuel cells and metal–air batteries.[25,26] The main limiting factor in the energy conversion efficiency of these devices is the sluggish ORR kinetics since ORR requires high overpotential and has a complex mechanism involving several steps.[27,28] ORR in alkaline media (such as in alkaline fuel cells) has faster kinetics, allowing the use of non-platinum (Pt) electrocatalysts in these cells.[29] Still, there are very few reports on $Ni(OH)_2$ activity for ORR; these previous studies typically involve supported $Ni(OH)_2$, transition metals (*e.g.*, Mn) coupled with $Ni(OH)_2$,[30] or $Ni(OH)_2$ supported on graphene oxide.[31,32] The activity of pure/unsupported $Ni(OH)_2$ electrocatalysts reported in those studies was rather modest.[31,32]

As mentioned above, nanostructured Ni-based materials can enhance the catalytic activity of electrochemical processes and long-term operation stability. Their physicochemical properties are determined by the synthesis conditions (reactants' concentrations, solvents used, surfactant templates, temperature, *etc.*) and significantly affect the material's electrical and electrochemical properties.[33] Thus, Ni-based materials of various morphologies (nanowires, nanoribbons),[34] nanorods, nanotubes,[35] nanosheets,[36] mesoporous structures,[37] hollow spheres[38] have been fabricated by different synthesis methods and tested for electrochemical applications.[39]

Herein, a hydrothermal method is used to produce $Ni(OH)_2$ nanoplatelets. The material was characterized by scanning (SEM) and transmission electron microscopy (TEM), X-ray diffraction (XRD) analysis, as well as by Raman and X-ray photoelectron (XPS) spectroscopy. Their multifunctional electrocatalytic performance was systematically investigated for ORR, OER, and HER in alkaline media.

2. Experimental

2.1. Synthesis of $Ni(OH)_2$

0.3 M $NiCl_2 \cdot 6H_2O$ was stirred in de-ionized (DI) water to obtain a uniform and clear solution. 35 mL of 2 M NaOH solution was added dropwise under constant stirring to form a $Ni(OH)_2$ suspension and kept for stirring for 2 h. Finally, the light green $Ni(OH)_2$ suspension was filtered and washed with DI water several times to remove Na^+ and Cl^- and other possible impurities. The filtered $Ni(OH)_2$ was added to 70 mL of 2.5 M NaOH solution and vigorously stirred for 30 min. Then, the suspension was transferred into a 100 mL Teflon-lined stainless steel autoclave, kept at 150 °C for 16 h in an electric oven, and then left to cool down to room temperature. The light green precipitate was obtained after centrifugation, thoroughly washed with DI water and ethanol alternately, several times until the filtrate pH became neutral. Finally, the product was dried in an electric oven overnight, at 80 °C.

2.2. Characterization methods

Scanning electron microscopy JSM-7001F (FEG of JEOL), operating in secondary electron imaging mode (SEI) with an applied voltage in the range of 10–15 kV, was used for the morphological characterization.

TEM of pure $Ni(OH)_2$ was performed using a Hitachi H8100 200 kV transmission electron microscope with a thermionic emission gun (LaB6).

XRD equipped with Cu Kα radiation ($\lambda = 0.15418$ nm) was used to study the crystallographic structure of $Ni(OH)_2$. The Scherrer equation (eqn (1)) was used to calculate the crystallite size,

$$D_\mathrm{p} = \frac{0.94\lambda}{\beta\cos\theta} \tag{1}$$

where D_p is the average crystallite size, β is line broadening in radians, θ is Bragg angle, λ is X-ray wavelength.

A micro-Raman spectrograph-Labram HR Evolution Raman spectrometer was used to characterize the $Ni(OH)_2$ material by irradiating a 532 nm laser beam with a laser power Pl = 0.054 mW to avoid overheating on the spot.

XPS spectra for $Ni(OH)_2$ were acquired in constant analyzer energy (CAE) mode (30 eV), using an Al (non-monochromatic) anode. The accelerating voltage was 15 kV. The deconvolution of the XPS spectra was done using Avantage® software. All spectra were referred to C 1s at 284.7 eV.

2.3. Electrochemical measurements

Oxygen reduction, hydrogen evolution, and oxygen evolution reactions were studied. Electrochemical measurements were undertaken in a conventional three-electrode cell using the AUTOLAB electrochemical workstation. A graphite rod was used as a counter electrode, and an Ag/AgCl/KCl electrode was used as a reference. All measured potentials were converted to the reversible hydrogen electrode (RHE) scale. A glassy carbon disk electrode ($0.19625\ cm^2$) coated by catalyst ink (5 μL of 5 mg in 125 μL of 2 wt% polyvinylidene fluoride solution in *N*-methyl-2-pyrrolidone) was used as the working electrode.

Cyclic voltammetry (CV) measurements were run in nitrogen (N_2)-saturated 1 M KOH electrolyte solution at rates of 10–100 mV s^{-1}. Linear sweep voltammetry (LSV) for ORR study was carried out in 1 M KOH solution saturated with high purity O_2 at polarization rate of 5 mV s^{-1} and electrode rotation rates of 0, 400, 600, 800, 1000, 1200, 1400, 1600, 1800, 2000, 2200, and 2400 rpm. LSVs for OER and HER were carried out in 1 M KOH solution at a rate of 5 mV s^{-1} at temperatures of 25–75 °C. IR-compensation was done to minimize the influence of solution resistance (conductivity) on catalytic performance. Electrochemical impedance spectroscopy (EIS) was performed using Gamry interface 5000E for the electrode at open circuit potential (OCP) in the frequency range from 100 kHz to 0.01 Hz at an RMS amplitude of 10 mV. Chronoamperometric measurements were run under HER (−0.3 V *vs.* RHE) and OER (1.68 V *vs.* RHE) polarization conditions for 2 h.

3. Results and discussion

3.1. Characterization of the materials

Fig. 1 shows the morphology of Ni(OH)$_2$, which consists of nanoplates with sizes ranging from 30 to 100 nm, uniformly distributed. As demonstrated by Banfield *et al.*,[40] the aggregation-based growth mechanism in the hydrothermal treatment drives the bulky precipitate of Ni(OH)$_2$ nanoparticles to form a nano platelet-like morphology. In this particular process, the particles in the absence of any inorganic or organic templates start to flocculate, forming colloidal aggregates. Under hydrothermal conditions of high temperature and pressure, these aggregates undergo rapid Brownian motion-driven collisions, which result in the elimination of water molecules with the formation of nickel–oxygen bonds and the development of the plate-like morphology.[41] It is worth pointing out that this nanoplatelet morphology was obtained without using any surfactants and structural templates, eliminating extra steps necessary to remove these structure-directing reagents and reducing structural damages.

Fig. 2a and b depicts the TEM images for Ni(OH)$_2$ obtained at different magnifications where the nanoplatelets like morphology oriented in random directions can be seen. The nanoplatelets seem thin and uniformly distributed in good agreement with the SEM results. The selected area diffraction (SAED) pattern (Fig. 2c) reveals spotted rings from Bragg reflection from individual crystallites, confirming the poly-nano-crystallinity of the material.

The crystal structure and phase information in the Ni(OH)$_2$ were obtained by XRD (Fig. 3a). The well-defined diffraction peaks at 2θ values of 19.2°, 33.02°, 38.48°, 52.07°, 58.97°, 62.6°, 70.42°, and 72.7° correspond to (001), (100), (101), (102), (110), (111), (103), and (201) planes, respectively, of hexagonal β-Ni(OH)$_2$ (JCPDS no.: 014-0117)[42] confirming the formation of high purity Ni(OH)$_2$ nanocrystals. The most intense peak at 19.2°, which shows the formation of β-Ni(OH)$_2$, was used to calculate the crystallite size using the Scherrer equation (eqn (1)). An average crystallite size of 31 nm was estimated, consistent with the SEM and TEM results.

Ni(OH)$_2$ was further characterized by Raman spectroscopy in the 200–800 cm^{-1} range (Fig. 3b). Raman stretching modes in low wavenumber are generally associated with metal-oxides/hydroxides. The peak at 310.78 cm^{-1} was attributed to the E-type vibration of the Ni–OH lattice. The peak at 444.98 cm^{-1} was assigned to the Ni–O stretching (υNiO).[43] In conclusion, both XRD and Raman spectrum demonstrate the formation of pure β-Ni(OH)$_2$.

XPS analyses were carried out to further check the chemical composition, and the results are depicted in Fig. 3c and d. The Ni 2p XPS photoionizations (Fig. 3c) evidenced two major peaks with binding energies at 856.21 and 873.81 eV, corresponding to Ni 2p$_{3/2}$ and Ni 2p$_{1/2}$, respectively.[44,45] These two peaks are separated by spin energy of 17.6 eV, which is characteristic of the Ni(OH)$_2$ phase, in good agreement with the reported data.[46] The peaks at 862.0 and 880.1 eV are associated with satellite peaks expected for Ni 2p$_{3/2}$ and Ni 2p$_{1/2}$ signals in the Ni 2p region. The O 1s spectra, Fig. 3d, evidenced a peak at a binding energy of 529.4 eV, which can be ascribed to the typical metal–oxygen bond of Ni–O.[47] The peak at 530.5 eV is usually associated with oxygen in OH$^-$ anions.[48] All the results obtained from XRD, Raman, and XPS confirm the formation of Ni(OH)$_2$.

3.2. Electrocatalysis by Ni(OH)$_2$

Electrochemical characterization of Ni(OH)$_2$ by CV in deaerated 1 M KOH (Fig. 4a) evidences the rise of a distinctive peak corresponding to β-Ni(OH)$_2$ conversion to NiOOH at a potential above 1.6 V in the first scan, as well as a pair of less intense redox peaks at *ca.* 1.3–1.5 V corresponding to the Ni^{2+}/Ni^{3+} redox couple in the subsequent scans.[49] Double-layer capacitance (C_{dl}) was determined from the voltammograms recorded in the potential region where no faradaic processes occur, Fig. 4b. A relatively high C_{dl} (0.1 mF cm^{-2}) value can be correlated to

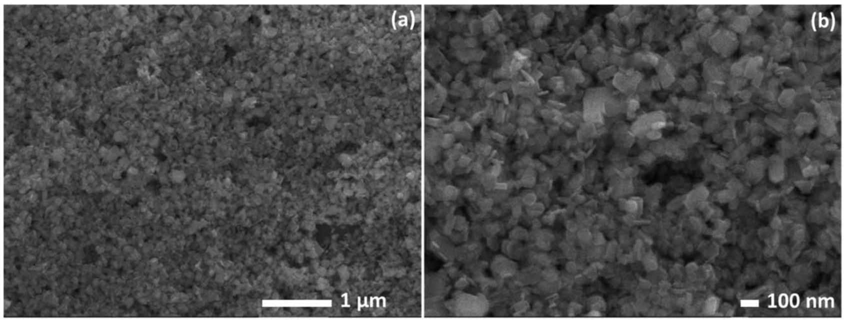

Fig. 1 SEM images of Ni(OH)$_2$ at different magnifications (a and b).

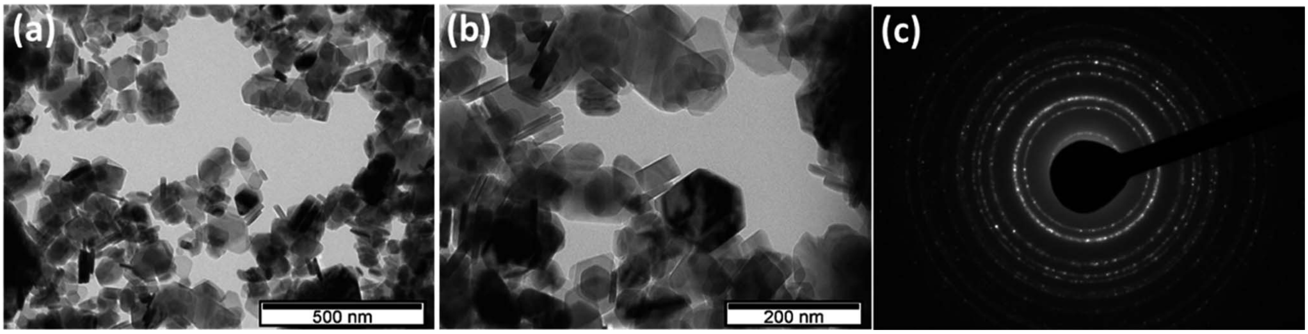

Fig. 2 TEM images (a and b) and SAED (c) for $Ni(OH)_2$.

a large electrochemical surface area (ECSA) and a high number of active sites for electrocatalysis. Namely, C_{dl} value was further used for the evaluation of ECSA and roughness factor (R) defined as the ratio of ECSA and the geometric area of the electrode (A), *i.e.*, the ratio of C_{dl} and the specific capacitance (C_s) of a standard, flat sample. As the theoretical value of C_s for $Ni(OH)_2$ is unknown, a C_s value of 25 μF cm^{-2} for a Ni electrode was used.[16] Roughness factor value of 4 for herein prepared $Ni(OH)_2$ evidences high ECSA, despite being lower than that reported for $Ni(OH)_2$ nanoparticles ($R = 16$).[16]

The accessibility of the active sites and their oxidation state will further influence the electrocatalytic reactivity. Namely, accessibility plays an essential role during OER as OER typically proceeds within a thin layer (*e.g.*, 10 nm) of the electrocatalyst.[50] Active sites in their higher oxidation state are further beneficial for OER, with this conversion to a higher oxidation state

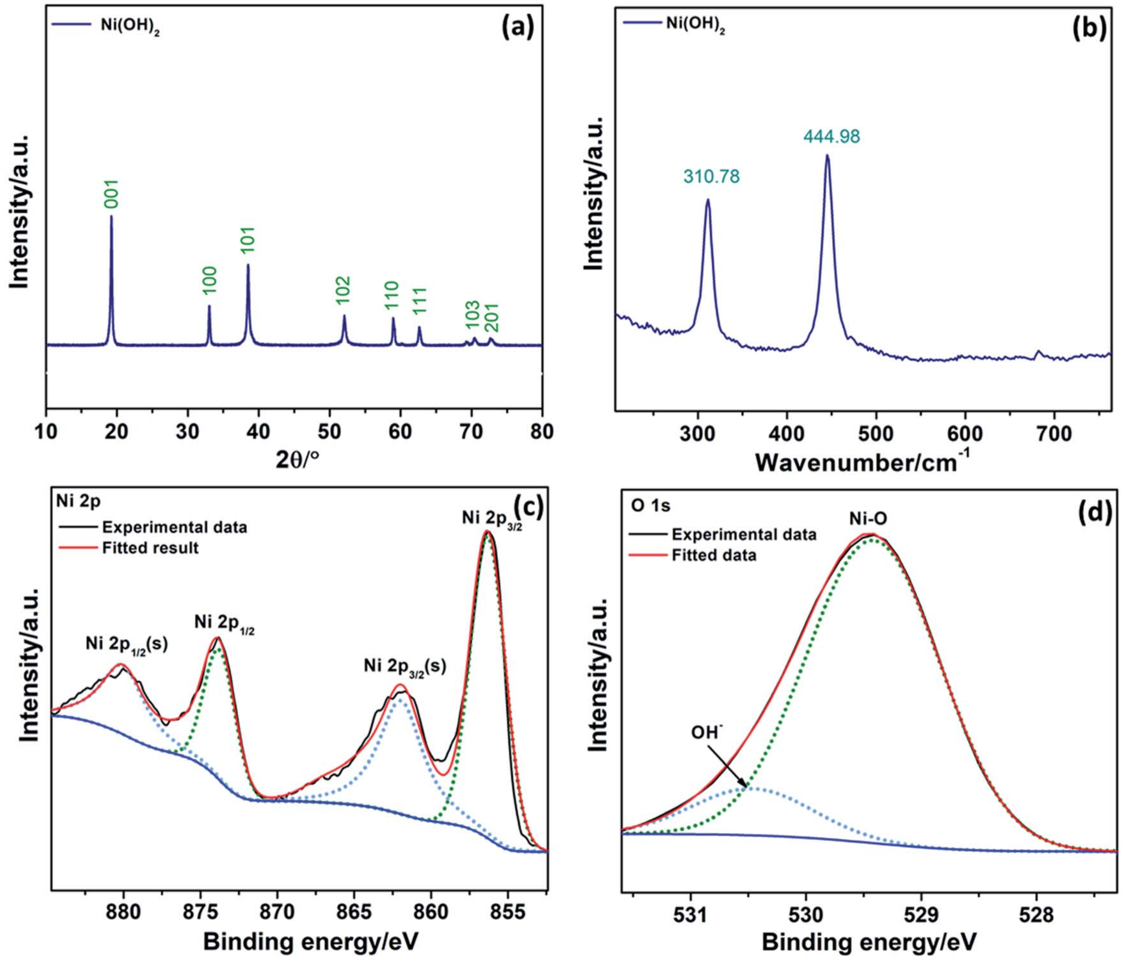

Fig. 3 XRD (a) and Raman spectra (b) of $Ni(OH)_2$. XPS spectra of Ni 2p (c) and O 1s (d) for $Ni(OH)_2$.

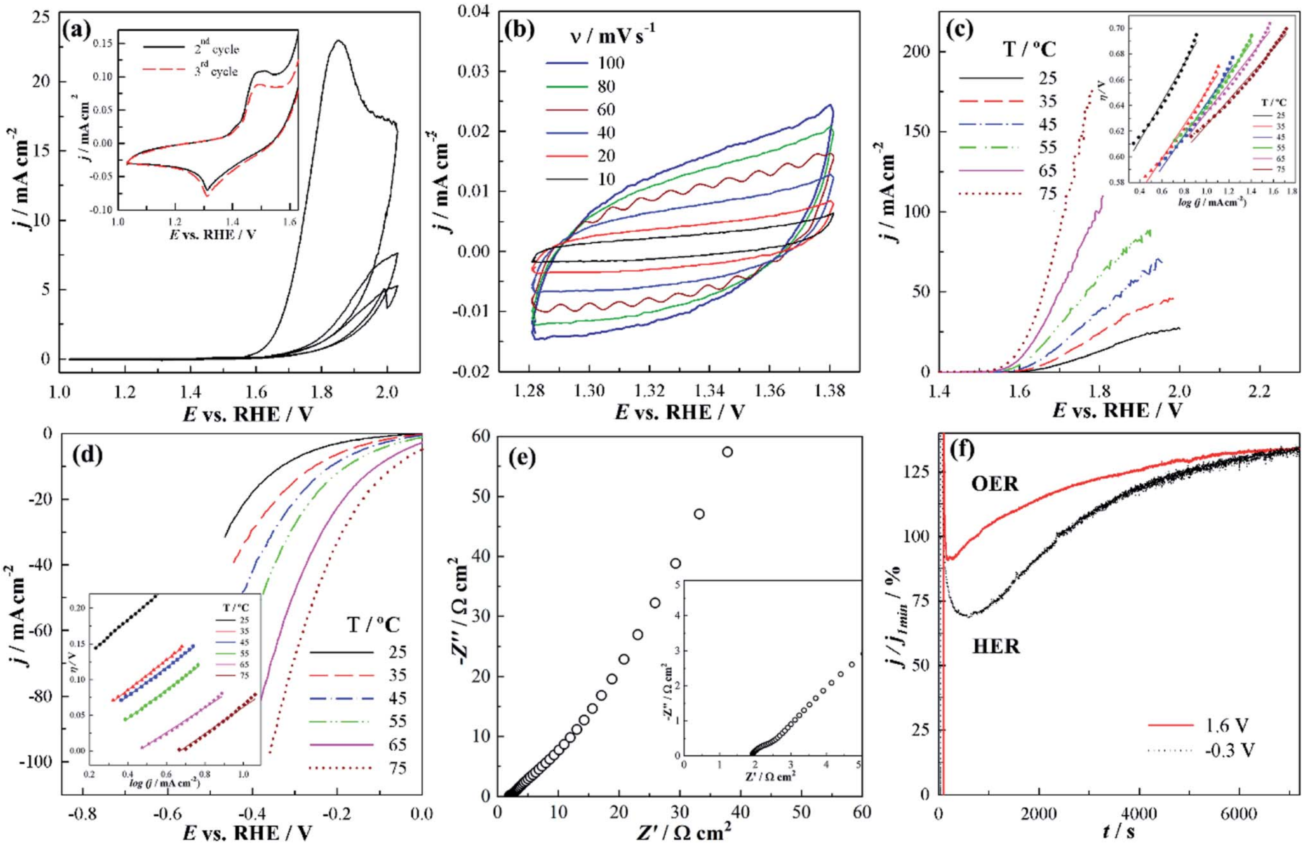

Fig. 4 Three consecutive CV curves of β-$Ni(OH)_2$ at 10 mV s^{-1} with lower-potential region of 2nd and 3rd cycle in inset (a) and CV curves at different polarization rates (b) in deaerated 1 M KOH. OER (c) and HER (d) polarization curves in 1 M KOH with the corresponding Tafel plots in the inset. Nyquist plots in 1 M KOH at OCP with the high-frequency region in inset (e). Chronoamperometric curves under OER (1.6 V) and HER (−0.3 V) polarization conditions in 1 M KOH (f).

occurring at potentials lower than OER. Combining a large contact area with electrolyte and the short ion-diffusion distance, along with a low charge transfer resistance, leads to higher electrocatalytic activity. In this case, a very low charge transfer resistance value of *ca.* 0.7 Ω cm^2 was obtained from the small semi-circle in the high-frequency region (inset of Fig. 4e), evidencing the good conductivity of the material.

LSV curve under anodic polarization conditions (Fig. 4c) reveals low OER onset potential (potential to reach a current density of 1 mA cm^{-2}) of 1.627 V at 25 °C, further leading to an overpotential of 0.498 V to reach a current density of 10 mA cm^{-2}. Thus, the overpotential to reach 1 mA cm^{-2} (reflecting the onset potential) at the herein prepared $Ni(OH)_2$ is comparable/lower than those previously reported for $Ni(OH)_2$ and $NiM(OH)_2$ (M = Cr, Mn, Cu, Co, Fe, Zn) electrocatalysts ranging from 0.290 V to over 0.500 V.[51] Overpotentials at 10 mA cm^{-2} for OER at different $Ni(OH)_2$-based electrocatalysts have been reported to be 0.331 V for β-$Ni(OH)_2$ NPs,[16] over 0.444 V for β-$Ni(OH)_2$ hexagonal NPs,[52] 0.474 V for β-$Ni(OH)_2$ nanoplate/MWCNT,[35] to 0.700 V for γ-$Ni(OH)_2$.[53] Furthermore, the reaction kinetics was found to notably improve with the increase of temperature with consequent reduction of overpotential to reach 10 mA cm^{-2} for *ca.* 80 mV.

In addition, Tafel analysis was used to evaluate the OER kinetics at this catalyst. OER on $Ni(OH)_2$ electrocatalysts has been suggested to involve a chemical association step between OH_{ads} and OH^- (eqn (3)) along with two electrochemical steps, *i.e.*, OH^- discharge (eqn (2)) and O_{ads}^- discharge (eqn (4)), followed by O_{ads} desorption to form molecular O_2 (eqn (5)):[54]

$$OH^- \leftrightarrow OH_{ads} + e^- \tag{2}$$

$$OH_{ads} + OH^- \leftrightarrow O_{ads}^- + H_2O \tag{3}$$

$$O_{ads}^- \leftrightarrow O_{ads} + e^- \tag{4}$$

$$2O_{ads} \leftrightarrow O_2 \tag{5}$$

with the overall reaction being given by eqn (6).

$$4OH^- \leftrightarrow O_2 + 2H_2O + 4e^- \tag{6}$$

Tafel slope *b* of 149 mV dec^{-1} at 25 °C decreasing to 99 mV dec^{-1} at 75 °C was determined for OER at $Ni(OH)_2$, Table 1. Tafel slope values at different α-$Ni(OH)_2$ and β-$Ni(OH)_2$ electrocatalysts were reported to range from 42 mV dec^{-1} for α-$Ni(OH)_2$ nanospheres[52] and α-$Ni(OH)_2$ hollow nanospheres[33] to

Table 1 OER parameters at $Ni(OH)_2$ at different temperatures

T/°C	E_{onset}/V	η_{10}/V	b/mV dec^{-1}	j_0/mA cm^{-2}
25	1.623	0.498	149	84.6
35	1.630	0.486	131	85.6
45	1.625	0.417	126	83.0
55	1.625	0.453	119	81.7
65	1.626	0.453	111	82.4
75	1.631	0.453	99	83.7

161 mV dec^{-1} for α-$Ni(OH)_2$ at Ni foam,[55] suggesting good electrocatalytic activity of the herein prepared β-$Ni(OH)_2$ nanoplatelets towards OER. Furthermore, a high exchange current density of *ca.* 85 mA cm^{-2} was recorded, Table 1.

Next, the electrocatalytic activity of $Ni(OH)_2$ toward HER in alkaline media was evaluated. Cathodic polarization curves at 25 °C (Fig. 4d) reveal a low HER onset potential of −0.101 V so that $Ni(OH)_2$ could reach −10 mA cm^{-2} at an overpotential of −0.333 V. A Tafel slope of −230 mV dec^{-1} was evaluated at 25 °C, decreasing to a value of −184 mV dec^{-1} with the increase of temperature, Table 2. Lower Tafel values have been reported upon doping $Ni(OH)_2$ with Fe.[19] Enhancement of the Ni-based materials electrocatalytic activity towards OER by introducing a second metal has been previously reported,[56] resulting from the modification of intermediate bonds and electronic structures, and consequent enhancement of the electric conductivity. This suggests two possible pathways for further improvement of the herein prepared $Ni(OH)_2$ electrocatalytic performance – doping with other metals, such as Fe or Co, or grafting onto conductive support such as reduced graphene oxide.[57]

Along with high electrocatalytic activity, stability and durability are crucial features for electrocatalyst's application in water electrolyzers. Chronoamperometric measurements in alkaline media demonstrated that β-$Ni(OH)_2$ electrocatalyst retains its catalytic activity towards OER and HER with time (Fig. 4f). Moreover, data shows an increase in current density with time. The improvement of reaction kinetics during the long stability tests has been previously reported for OER and HER in both alkaline[58,59] and acidic[60] media. The increase in current density suggests that as $Ni(OH)_2$ is preserved in alkaline media, inner regions of the material become accessible to the electrolyte with time.[59]

Table 2 HER parameters at β-$Ni(OH)_2$ at different temperatures

T/°C	E_{onset}/V	η_{10}/V	b/mV dec^{-1}	j_0/mA cm^{-2}
25	−0.102	−0.333	−230	0.402
35	−0.053	−0.256	−211	0.991
45	−0.028	−0.217	−202	1.051
55	0.002	−0.181	−203	1.510
65	0.047	−0.109	−184	2.913
75	0.092	−0.065	−204	4.852

Finally, the performance of β-$Ni(OH)_2$ for ORR was evaluated. The onset potential was found to be 0.73 V, comparable to that of freeze-dried Ni/NiO_x (0.75 V) and more positive than those of freeze-dried $Ni(OH)_2$ (0.66 V) and NiO (Fig. 5a, and Table 3).[61] Similarly, ORR half-wave potential at $Ni(OH)_2$ was found to be comparable/more positive than those of freeze-dried Ni/NiO_x (0.62 V), freeze-dried $Ni(OH)_2$ (0.56 V), and NiO (0.55 V).

Tafel analysis of the mass transfer-corrected ORR polarization curves at a rotation rate of 1800 rpm (Fig. 5a) revealed a Tafel slope of −78 mV dec^{-1}, comparable to that of commercial Pt/C (40 wt% Pt) (−79 and −60 mV dec^{-1}, depending on the potential region) (Table 3).[62] Mn_2O_3–NiO also showed two Tafel regions with slopes of −75 mV dec^{-1} and −103 mV dec^{-1}.[62] A higher Tafel slope value of −95 mV dec^{-1} was reported for ORR at $NiCoO_2$,[63] which indicates the better catalytic performance of herein prepared $Ni(OH)_2$ (Table 3).

The number of exchanged electrons, n, was determined by Koutecky–Levich analysis, and the obtained n values ranged between 3 and 4, depending on the potential (Fig. 5 and Table 1). These values suggest that ORR at $Ni(OH)_2$ nanoplatelets proceeds by both 4e$^-$-mechanism (eqn (7)) and 2e− mechanism (eqn (8)), with the desirable direct 4e$^-$-reduction of O_2 being the dominant one.

$$O_2 + 2H_2O + 4e^- \rightarrow 4OH^- \tag{7}$$

$$O_2 + H_2O + 2e^- \rightarrow HO_2^- + OH^- \tag{8}$$

Study of ORR on α-$Ni(OH)_2$ and α-$Ni(OH)_2$ supported on graphene oxide revealed transfer of a lower number of 2.9 ± 0.2 electrons for unsupported α-$Ni(OH)_2$, regardless of the NaOH concentration, and transfer of 3.4 to 3.9 electrons at GO-supported α-$Ni(OH)_2$, depending on the NaOH concentration.[32] Similarly, only 2.1 electrons were exchanged during ORR at a microwave synthesized α-$Ni(OH)_2$ and 3.5 electrons on such prepared $Ni(OH)_2$ on graphene oxide.[31] Furthermore, ORR limiting current densities at the herein studied $Ni(OH)_2$ were observed to be higher than those recorded at microwave synthesized α-$Ni(OH)_2$.[31] Higher ORR kinetics at the GO-supported $Ni(OH)_2$ was attributed to a lower activation energy for O_2 adsorption.[32] ORR was found to be a first-order reaction with respect to oxygen, *i.e.*, the adsorption of oxygen was indicated to be the rate-determining step at both unsupported and GO-supported $Ni(OH)_2$.[32] It can be speculated that herein synthesized $Ni(OH)_2$ nanoplatelets show higher performance than unsupported $Ni(OH)_2$ due to a similar reaction mechanism but lower activation energy for O_2 adsorption.

Considering evaluated ORR parameters, herein prepared $Ni(OH)_2$ exhibits noteworthy ORR activity that overpasses the activity of a few previously explored $Ni(OH)_2$ electrocatalysts in terms of higher limiting current density and higher number of exchanged electrons.[31,32] Given the good electrocatalytic performance of $Ni(OH)_2$ towards OER, HER, and ORR in alkaline media, as well as high stability, the next step would be to evaluate this material in an alkaline water electrolyzer

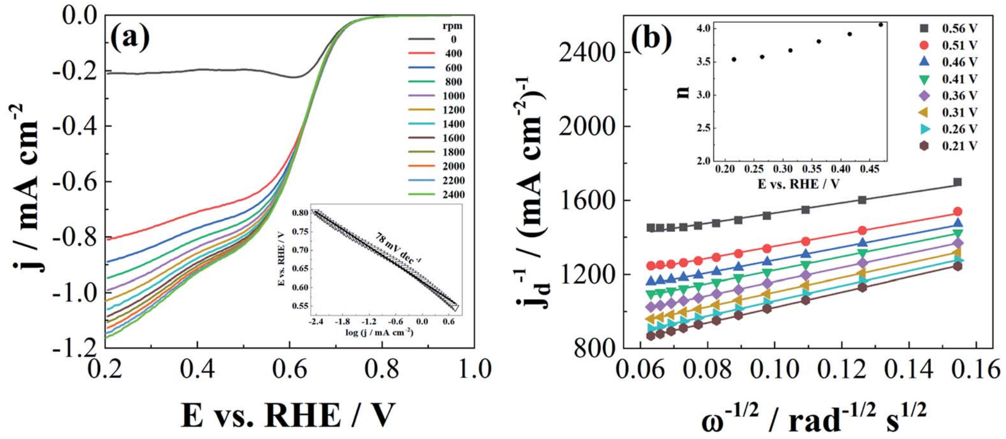

Fig. 5 LSV curves in O_2-saturated 1 M KOH at different rotation rates with Tafel plot at 1800 rpm in inset (a) and corresponding Koutecky–Levich plots at different potentials with the number of exchanged electrons in inset (b).

Table 3 ORR parameters for $Ni(OH)_2$ nanoplatelets and some previously reported catalysts

Material	Morpho-logy	Crystallite/particle size/nm	Electrolyte	b/mV dec^{-1}	n	$E_{1/2}$/V	E_{on}/V	Source
$Ni(OH)_2$	Nanoplates	30–100	0.1 M KOH	78	4.01	0.63	0.72	This work
Freeze-dried $Ni(OH)_2$	Layered	–	1 M KOH	–	–	0.56	0.66	61
NiO	–	–	1 M KOH	–	–	0.55	0.65	61
Freeze-dried Ni/NiO_x	–	–	1 M KOH	–	3.75	0.62	0.75	61
α-$Ni(OH)_2$	Rhombohedral particle	250–300	0.05–0.5 M NaOH	–	2.9 ± 0.2	–	–	32
α-$Ni(OH)_2$/GO	Rhombohedral particles and platelets	150–200	0.05–0.5 M NaOH	–	3.4 to 3.9	–	–	32
$Ni(OH)_2$	Rhombohedral particle	250–300	0.5 M NaOH	—	2.1	—	0.75	31
$Ni(OH)_2$/GO	Rhombohedral particles and platelets	150–200	0.5 M NaOH	–	3.5	–	0.83	31
Mn_2O_3–NiO	–	–	0.1 M KOH	75, 103	3.89	–	–	62
$NiCoO_2$	–	13		95	3.86	0.79	0.85	63
Pt/C (40 wt% Pt)	Nanopatricles	–	0.1 M KOH	79, 60	3.96	0.92	0.96	62

with $Ni(OH)_2$ as both anode and cathode electrocatalyst, and a fuel cell or metal–air battery with $Ni(OH)_2$ cathode electrocatalyst.

4. Conclusions

In summary, β-$Ni(OH)_2$ nanoplatelets of *ca.* 31 nm average size have been produced *via* a hydrothermal method and tested as multifunctional electrocatalysts for alkaline water electrolysis and oxygen reduction reaction. The pristine β-$Ni(OH)_2$ demonstrated high electrocatalytic activity towards OER, characterized by a Tafel slope of 149 mV dec^{-1} (decreasing to 99 mV dec^{-1} at 75 °C) and an overpotential of 498 mV at 25 °C to reach a current density of 10 mA cm^{-2}. Additionally, high HER catalytic performance was observed with a Tafel slope of −230 mV dec^{-1} and a current density of 10 mA cm^{-2} at an overpotential of −333 mV at 25 °C, decreasing to −65 mV at 75 °C. High stability in alkaline media under both anodic and cathodic polarization conditions was confirmed. Finally, the synthesized catalyst showed high electrocatalytic activity towards ORR, with a low Tafel slope (−78 mV dec^{-1}) and a number of exchanged electrons (4.01) corresponding to the direct 4e-mechanism. This outstanding result expressively surpasses the few previous reports on modest ORR activity of pure $Ni(OH)_2$. The obtained electrochemical data suggest that β-$Ni(OH)_2$ nanoplatelets are promising multifunctional electrocatalysts for ORR and water splitting in alkaline media for application in different electrochemical energy storage/conversion devices.

Author contributions

A. B. – investigation, formal analysis; K. K. U. – investigation, formal analysis, writing – original draft; K. R. – investigation, formal analysis, writing – original draft, D. M. F. S. – visualization, writing – review & editing, M. F. M. – conceptualization, supervision, writing – review & editing B. Š. – conceptualization; supervision, writing – original draft, writing – review & editing.

Conflicts of interest

There are no conflicts to declare.

Acknowledgements

The authors would like to thank Fundação para a Ciência e a Tecnologia (FCT, Portugal) (research contract in the scope of programmatic funding UIDP/04540/2020 (D. M. F. Santos), CQE – UIDB/00100/2020, UIDP/00100/2020, LA/P/0056/2020, and IST-ID/156-2018 (B. Šljukić)) as well as the Science Fund of the Republic of Serbia (PROMIS programme, RatioCAT, no. 606224).

References

1 Y. Miao, L. Ouyang, S. Zhou, L. Xu, Z. Yang, M. Xiao and R. Ouyang, *Biosens. Bioelectron.*, 2014, **53**, 428–439.
2 A. Safavi, N. Maleki and E. Farjami, *Biosens. Bioelectron.*, 2009, **24**, 1655–1660.
3 M. Vidotti, S. I. C. de Torresi and L. T. Kubota, *Sens. Actuators, B*, 2008, **135**, 245–249.
4 L. A. Hutton, M. Vidotti, A. N. Patel, M. E. Newton, P. R. Unwin and J. V. MacPherson, *J. Phys. Chem. C*, 2010, **115**, 1649–1658.
5 M. Aghazadeh, A. N. Golikand and M. Ghaemi, *Int. J. Hydrogen Energy*, 2011, **36**, 8674–8679.
6 S. Anantharaj, P. E. Karthik and S. Kundu, *Catal. Sci. Technol.*, 2017, **7**, 882–893.
7 J. W. Lee, J. M. Ko and J. D. Kim, *J. Phys. Chem. C*, 2011, **115**, 19445–19454.
8 I. C. Man, H. Y. Su, F. Calle-Vallejo, H. A. Hansen, J. I. Martínez, N. G. Inoglu, J. Kitchin, T. F. Jaramillo, J. K. Nørskov and J. Rossmeisl, *ChemCatChem*, 2011, **3**, 1159–1165.
9 F. Dionigi and P. Strasser, *Adv. Energy Mater.*, 2016, **6**, 1600621.
10 S. Klaus, Y. Cai, M. W. Louie, L. Trotochaud and A. T. Bell, *J. Phys. Chem. C*, 2015, **119**, 7243–7254.
11 J. Jiang, S. Lu, W. K. Wang, G. X. Huang, B. C. Huang, F. Zhang, Y. J. Zhang and H. Q. Yu, *Nano Energy*, 2018, **43**, 300–309.
12 M. Shalom, D. Ressnig, X. Yang, G. Clavel, T. P. Fellinger and M. Antonietti, *J. Mater. Chem. A*, 2015, **3**, 8171–8177.
13 C. Zhang, Y. Xie, H. Deng, C. Zhang, J. W. Su, Y. Dong and J. Lin, *Int. J. Hydrogen Energy*, 2018, **43**, 7299–7306.
14 A. T. Swesi, J. Masud and M. Nath, *Energy Environ. Sci.*, 2016, **9**, 1771–1782.
15 X. Xu, F. Song and X. Hu, *Nat. Commun.*, 2016, **7**, 12324.
16 L. A. Stern and X. Hu, *Faraday Discuss.*, 2014, **176**, 363–379.
17 S. Niu, W. J. Jiang, T. Tang, Y. Zhang, J. H. Li and J. S. Hu, *Adv. Sci.*, 2017, **4**, 1700084.
18 Y. Li, H. Zhang, M. Jiang, Q. Zhang, P. He and X. Sun, *Adv. Funct. Mater.*, 2017, **27**, 1–8.
19 J. T. Ren, G. G. Yuan, C. C. Weng, L. Chen and Z. Y. Yuan, *Nanoscale*, 2018, **10**, 10620–10628.
20 J. Milikić, M. Vasić, L. Amaral, N. Cvjetićanin, D. Jugović, R. Hercigonja and B. Šljukić, *Int. J. Hydrogen Energy*, 2018, **43**, 18977–18991.
21 H. Zhao and Z. Y. Yuan, *J. Energy Chem.*, 2021, **54**, 89–104.
22 C. Tang, R. Zhang, W. Lu, L. He, X. Jiang, A. M. Asiri and X. Sun, *Adv. Mater.*, 2016, **29**, 1602441.
23 X. H. Lucas-Alexandre Stern, L. Feng and F. Song, *Energy Environ. Sci.*, 2015, **8**, 2347.
24 B. You, N. Jiang, M. Sheng, M. W. Bhushan and Y. Sun, *ACS Catal.*, 2016, **6**, 714–721.
25 F. Cheng and J. Chen, *Chem. Soc. Rev.*, 2012, **41**, 2172–2192.
26 M. S. Dresselhaus and I. L. Thomas, *Nature*, 2001, **414**, 332–337.
27 H. Dong, B. Lin, K. Gilmore, T. Hou, S. T. Lee and Y. Li, *J. Power Sources*, 2015, **299**, 371–379.
28 J. A. Keith, G. Jerkiewicz and T. Jacob, *ChemPhysChem*, 2010, **11**, 2779–2794.
29 S. Mentus and D. M. F. Santos, *Nanomaterials*, 2020, **10**, 1805.
30 Q. Wu, L. Jiang, Q. Tang, J. Liu, S. Wang and G. Sun, *Electrochim. Acta*, 2013, **91**, 314–322.
31 E. Farjami, M. A. Rottmayer and L. Jay Deiner, *J. Mater. Chem. A*, 2013, **1**, 15501–15508.
32 E. Farjami and L. J. Deiner, *J. Electrochem. Soc.*, 2015, **162**, H571–H578.
33 L. Xu, Y. Ding, C. Chen, L. Zhao, C. Rimkus, R. Joesten and S. L. Suib, *Chem. Mater.*, 2008, **20**, 308–316.
34 D. Yang, R. Wang and M. He, *J. Phys. Chem. B*, 2005, **109**, 7654–7658.
35 X. Zhou, Z. Xia, Z. Zhang, Y. Ma and Y. Qu, *J. Mater. Chem. A*, 2014, **2**, 11799–11806.
36 L. Liu, Y. Li, S. Yuan, M. Ge, M. Ren, C. Sun and Z. Zhou, *J. Phys. Chem. C*, 2010, **114**, 251–255.
37 Z. Hongjun, A. Hagfeldt and G. Boschloo, *J. Phys. Chem. C*, 2007, **111**, 17455–17458.
38 Y. Wang, Q. Zhu and H. Zhang, *Chem. Commun.*, 2005, 5231–5233.
39 D. Wang, W. Yan and G. G. Botte, *Electrochem. Commun.*, 2011, **13**, 1135–1138.
40 J. F. Banfield, S. A. Welch, H. Zhang, T. T. Ebert and R. L. Penn, *Science*, 2000, **289**, 751–754.
41 J. C. Yu, A. Xu, L. Zhang, R. Song and L. Wu, *J. Phys. Chem. B*, 2004, **108**, 64–70.
42 C. Li and S. Liu, *J. Nanomater.*, 2020, **10**, 1805.
43 X. Xiong, D. Ding, D. Chen, G. Waller, Y. Bu, Z. Wang and M. Liu, *Nano Energy*, 2015, **11**, 154–161.
44 J. Yan, Z. Fan, W. Sun, G. Ning, T. Wei, Q. Zhang, R. Zhang, L. Zhi and F. Wei, *Adv. Funct. Mater.*, 2012, **22**, 2632–2641.
45 K. S. Kim and N. Winograd, *Surf. Sci.*, 1974, **43**, 625–643.
46 J. W. Lee, T. Ahn, D. Soundararajan, J. M. Ko and J. D. Kim, *Chem. Commun.*, 2011, **47**, 6305–6307.
47 G. Zhou, D. W. Wang, L. C. Yin, N. Li, F. Li and H. M. Cheng, *ACS Nano*, 2012, **6**, 3214–3223.
48 A. A. Khaleed, A. Bello, J. K. Dangbegnon, M. J. Madito, O. Olaniyan, F. Barzegar, K. Makgopa, K. O. Oyedotun, B. W. Mwakikunga, S. C. Ray and N. Manyala, *J. Alloys Compd.*, 2017, **721**, 80–91.
49 D. M. F. Santos, L. Amaral, B. Šljukić, D. Macciò, A. Saccone and C. A. C. Sequeira, *J. Electrochem. Soc.*, 2014, **161**, F386–F390.
50 J. P. Kumar, S. D. Giri and A. Sarkar, *Int. J. Hydrogen Energy*, 2018, **43**, 15639–15649.
51 O. Diaz-Morales, I. Ledezma-Yanez, M. T. M. Koper and F. Calle-Vallejo, *ACS Catal.*, 2015, **5**, 5380–5387.

52 M. Gao, W. Sheng, Z. Zhuang, Q. Fang, S. Gu, J. Jiang and Y. Yan, *J. Am. Chem. Soc.*, 2014, **136**, 7077–7084.

53 B. S. Yeo and A. T. Bell, *J. Phys. Chem. C*, 2012, **116**, 8394–8400.

54 X. Wang, H. Luo, H. Yang, P. J. Sebastian and S. A. Gamboa, *Int. J. Hydrogen Energy*, 2004, **29**, 967–972.

55 G. Liu, Z. Sun, X. Zhang, H. Wang, G. Wang, X. Wu, H. Zhang and H. Zhao, *J. Mater. Chem. A*, 2018, **6**, 19201–19209.

56 M. Tahir, L. Pan, F. Idrees, X. Zhang, L. Wang, J. J. Zou and Z. L. Wang, *Nano Energy*, 2017, **37**, 136–157.

57 K. K. Upadhyay, N. Bundaleska, M. Abrashev, N. Bundaleski, O. M. N. D. Teodoro, I. Fonseca, A. M. de Ferro, R. P. Silva, E. Tatarova and M. F. Montemor, *Electrochim. Acta*, 2020, **334**, 135592.

58 J. Yu, S. Pan, Y. Zhang, Q. Liu and B. Li, *Front. Mater.*, 2019, **6**, 124.

59 B. Šljukić, D. M. F. Santos, M. Vujković, L. Amaral, R. P. Rocha, C. A. C. Sequeira and J. L. Figueiredo, *ChemSusChem*, 2016, **9**, 1200–1208.

60 B. Šljukić, M. Vujković, L. Amaral, D. M. F. Santos, R. P. Rocha, C. A. C. Sequeira and J. L. Figueiredo, *J. Mater. Chem. A*, 2015, **3**, 15505–15512.

61 Y. Shudo, M. Fukuda, M. S. Islam, K. Kuroiwa, Y. Sekine, M. R. Karim and S. Hayami, *Nanoscale*, 2021, **13**, 5530–5535.

62 D. Mladenović, D. M. F. Santos, G. Bozkurt, G. S. P. Soylu, A. B. Yurtcan, Š. Miljanić and B. Šljukić, *Electrochem. Commun.*, 2021, **124**, 106963.

63 A. Ashok, A. Kumar, J. Ponraj, S. A. Mansour and F. Tarlochan, *Int. J. Hydrogen Energy*, 2019, **44**, 16603–16614.